



RESEARCH LETTER

10.1002/2017GL073627

Key Points:

- Decomposition of InSAR data reveals spatial variations of uplift rates on folds in the foreland of the Tian Shan and Pamir in NW China
- Piecewise linear fits to geodetic and geologic uplift rates constrain temporal evolutions of uplift rates on five active folds
- Our observations confirm propagation of deformation from the Tian Shan and Pamir mountain fronts into the Tarim Basin

Supporting Information:

- Data Set S1
- Data Set S2
- Supporting Information S1
- Table S1

Correspondence to:

A. Bufe,
 abufe@gfz-potsdam.de

Citation:

Bufe, A., D. P. S. Bekaert, E., Hussain, B. Bookhagen, D. W. Burbank, J. A. Thompson Jobe, J. Chen, T. Li, L. Liu, and W. Gan (2017), Temporal changes in rock uplift rates of folds in the foreland of the Tian Shan and the Pamir from geodetic and geologic data, *Geophys. Res. Lett.*, 44, 10,977–10,987, doi:10.1002/2017GL073627.

Received 7 FEB 2017

Accepted 23 MAY 2017

Accepted article online 31 MAY 2017

Published online 14 NOV 2017

Temporal changes in rock uplift rates of folds in the foreland of the Tian Shan and the Pamir from geodetic and geologic data

Aaron Bufe^{1,2,3} , David P. S. Bekaert⁴ , Ekbal Hussain⁵ , Bodo Bookhagen^{2,6} , Douglas W. Burbank^{1,2} , Jessica A. Thompson Jobe^{2,7} , Jie Chen⁸, Tao Li^{8,9}, Langtao Liu^{8,10}, and Weijun Gan⁸

¹Department of Earth Sciences, University of California, Santa Barbara, California, USA, ²Earth Research Institute, University of California, Santa Barbara, California, USA, ³Now at GFZ German Research Center for Geosciences, Potsdam, Germany, ⁴Jet Propulsion Laboratory, California Institute of Technology, Pasadena, California, USA, ⁵School of Earth and Environment, University of Leeds, Leeds, UK, ⁶Institute of Earth and Environmental Science, University of Potsdam, Potsdam-Golm, Germany, ⁷Institute of Tectonic Studies, Department of Geological Sciences, University of Texas, El Paso, Texas, USA, ⁸State Key Laboratory of Earthquake Dynamics, Institute of Geology, China Earthquake Administration, Beijing, China, ⁹School of Earth Science and Engineering, Sun Yat-Sen University, Guangzhou, China, ¹⁰Department of Earth Science and Engineering, Hebei University of Engineering, Handan, China

Abstract Understanding the evolution of continental deformation zones relies on quantifying spatial and temporal changes in deformation rates of tectonic structures. Along the eastern boundary of the Pamir-Tian Shan collision zone, we constrain secular variations of rock uplift rates for a series of five Quaternary detachment- and fault-related folds from their initiation to the modern day. When combined with GPS data, decomposition of interferometric synthetic aperture radar time series constrains the spatial pattern of surface and rock uplift on the folds deforming at decadal rates of 1–5 mm/yr. These data confirm the previously proposed basinward propagation of structures during the Quaternary. By fitting our geodetic rates and previously published geologic uplift rates with piecewise linear functions, we find that gradual rate changes over >100 kyr can explain the interferometric synthetic aperture radar observations where changes in average uplift rates are greater than ~1 mm/yr among different time intervals (~10¹, 10^{4–5}, and 10^{5–6} years).

1. Introduction

Deformation rates along individual tectonic structures underpin our understanding of the dynamics of continental deformation zones and their seismic hazards. Whereas the mechanics for many types of folds and faults are well understood [Suppe, 1983; Suppe and Medwedeff, 1990; Epard and Groshong, 1995; Poblet and McClay, 1996; Allmendinger, 1998; Li et al., 2013; Yan et al., 2016], commonly unknown temporal and spatial differences in deformation rates complicate the reconstruction of the kinematic history of their deformation. After initiation, faults and folds tend to lengthen with annual rates of lateral propagation ranging from a few millimeters to several centimeters [Burbank et al., 1996; Jackson et al., 2002; Chen et al., 2007], until they encounter barriers that pin the tips of the structure [Dawers et al., 1993; Manighetti et al., 2001; Amos et al., 2010]. Commonly, a near-block-like pattern of incremental (or instantaneous) slip is assumed with spatially constant slip rate along the structure, rapidly decreasing to 0 at the tips [Manighetti et al., 2001; Amos et al., 2010]. Nonetheless, block-like incremental slip is not necessary and spatially varying deformation rates have been shown to occur, for example, along laterally tilting folds [Li et al., 2013], propagating structures [Amos et al., 2010], or segmented ones [Dawers et al., 1993; Anders and Schlische, 1994; Davis et al., 2005]. In addition to spatial variations of slip rates, deformation varies temporally. Changes in the distribution of strain across fault zones and mountain ranges [Thompson et al., 2002; Oskin et al., 2007], foreland propagation of deformation [Hubert-Ferrari et al., 2007; Heermance et al., 2008], propagation of asperities along structures [Hilley and Arrowsmith, 2008], loading or unloading of the crust by water or ice [Hampel et al., 2007], or reorganization of strain across plate boundaries [Friedrich et al., 2003; Allen et al., 2004; Sobel et al., 2006; Molnar and Stock, 2009; Clark, 2012] can cause decadal to million-year variations in slip rates. Moreover, stochastic or cyclic temporal variations in deformation rates can occur due, for example, to the clustering of strain release [Grant and Sieh, 1994; Marco et al., 1996; Friedrich et al., 2003; Meade and Hager, 2004;

Dolan et al., 2007; Oskin et al., 2008], seasonal water loading [*Bettinelli et al., 2008*], or changes throughout a seismic cycle [*Thatcher, 1984; Cattin and Avouac, 2000; Hilley et al., 2009*].

Slip rate variations of single structures on geologic timescales are inferred from rate measurements across multiple time intervals and, in the absence of additional evidence, are commonly described as step-like changes [*Hubert-Ferrari et al., 2007; Oskin et al., 2007; Heermance et al., 2008; Gold and Cowgill, 2011; Gold et al., 2017*]. Whereas measuring gradual rate changes requires a data density that is commonly not available [*Gunderson et al., 2014*], an assumed functional form can be fitted to existing measurements [*Gourmelen et al., 2011*].

From a decomposition of interferometric synthetic aperture radar (InSAR) time series and GPS data, we constrain patterns of surface uplift rates for a series of Quaternary contractional structures along the rapidly deforming eastern boundary of the Pamir-Tian Shan collision zone. Assuming uplift of sparsely eroded surfaces to be equivalent to rock uplift, these data are then compared with geologic rates. In addition to fitting temporal changes in uplift rates with step functions, we impose piecewise linear functions of temporal uplift rate changes and explore a range of possible alternative velocity variations with a Monte Carlo model.

2. Geologic Setting

The Pamir and Tian Shan jointly accommodate 20–25 mm of shortening per year, nearly 50% of the total Indo-Asian shortening rate [*Abdrakhmatov et al., 1996; Zubovich et al., 2010*] (Figure 1). About 11 ± 3 mm/yr of present-day shortening is taken up across the $\sim 70 \pm 10$ km wide boundary between the two orogens (Figures 1a and 1b). At the eastern edge of the Pamir, deformation along the Main Pamir Thrust appears to have mostly ceased [*Chen et al., 2011; Sobel et al., 2011; Thompson et al., 2015*] and stepped northward, where it interferes with the southern Tian Shan (Figure 1c). Here the Pamir Frontal Thrust (PFT), the Mingyaole fold, and the Mushi fold accommodate a total Late Quaternary shortening of ~ 6 –7 mm/yr [*Li et al., 2012, 2013, 2015*]. To the east of the PFT, deformation along the Tarim Basin-Tian Shan boundary has stepped southward from the South Tian Shan Thrust into the Kashi foreland basin over the past 25 Myr, causing the initiation, growth, and abandonment of a series of southward younging structures (Figure 1c) [*Heermance et al., 2008*]. Modern deformation occurs on a series of anticlines: the Kashi, Atushi, and Mutule folds (Figure 1c) that have each accommodated >2 –3 mm/yr of shortening since their initiation 1–2 Myr ago [*Scharer et al., 2004; Chen et al., 2007*]. Structures to the north of these folds, such as the Keketamu and Tashipisake anticlines, lack deformed Late Quaternary surfaces and appear to be mostly inactive [*Heermance et al., 2008*].

3. Methods and Data

InSAR time series analysis of Envisat-advanced synthetic aperture radar (ASAR) data from two ascending tracks (55 and 284) and two descending tracks (191 and 420) was performed using the Stanford Method for Persistent Scatterers (StaMPS) [*Hooper et al., 2004, 2012*] (Figure S1 and Table S1 in the supporting information). Interferograms from the Envisat scenes acquired between 2003 and 2010 were generated using the ROI_PAC [*Rosen et al., 2004*] and DORIS [*Kampes and Usai, 1999*] packages, topography was removed with a 90 m resolution Shuttle Radar Topography Mission digital elevation model [*Farr et al., 2007*], and atmospheric phase delays were corrected with the Toolbox for Reducing Atmospheric InSAR Noise (TRAIN) [*Dee et al., 2011; Bekaert et al., 2015a, 2015b*] (Figures S2–S4). An interpolated northward velocity field from published GPS data [*Zubovich et al., 2010*], together with ascending and descending InSAR time series, was then used to reference the InSAR velocities to stable Eurasia and to decompose the geodetic data into eastward and vertical components (Figures S3 and S4) [*Hussain et al., 2016a, 2016b*] (see Text S1 for additional detail). In the remainder of the analysis, we use only the decomposed vertical velocity field as a measure of absolute decadal surface uplift rates. Peak decadal surface uplift rates were measured on 10 km wide swath profiles plotted approximately perpendicular to the strike of thrust faults and/or the trend of fold axes (Figures S5–S7 and Table S2). The weighted arithmetic means and corresponding standard errors were calculated in 1 km bins along the length of the 10 km wide swath profiles. Decadal peak uplift rates were then specified as the maximum of the binned InSAR velocities across each structure. Where the InSAR data are coherent, significant erosion or sedimentation is unlikely. Therefore, the resulting decadal surface uplift rates of major tectonic structures are assumed to largely reflect absolute rates of rock uplift with respect to stable Eurasia.

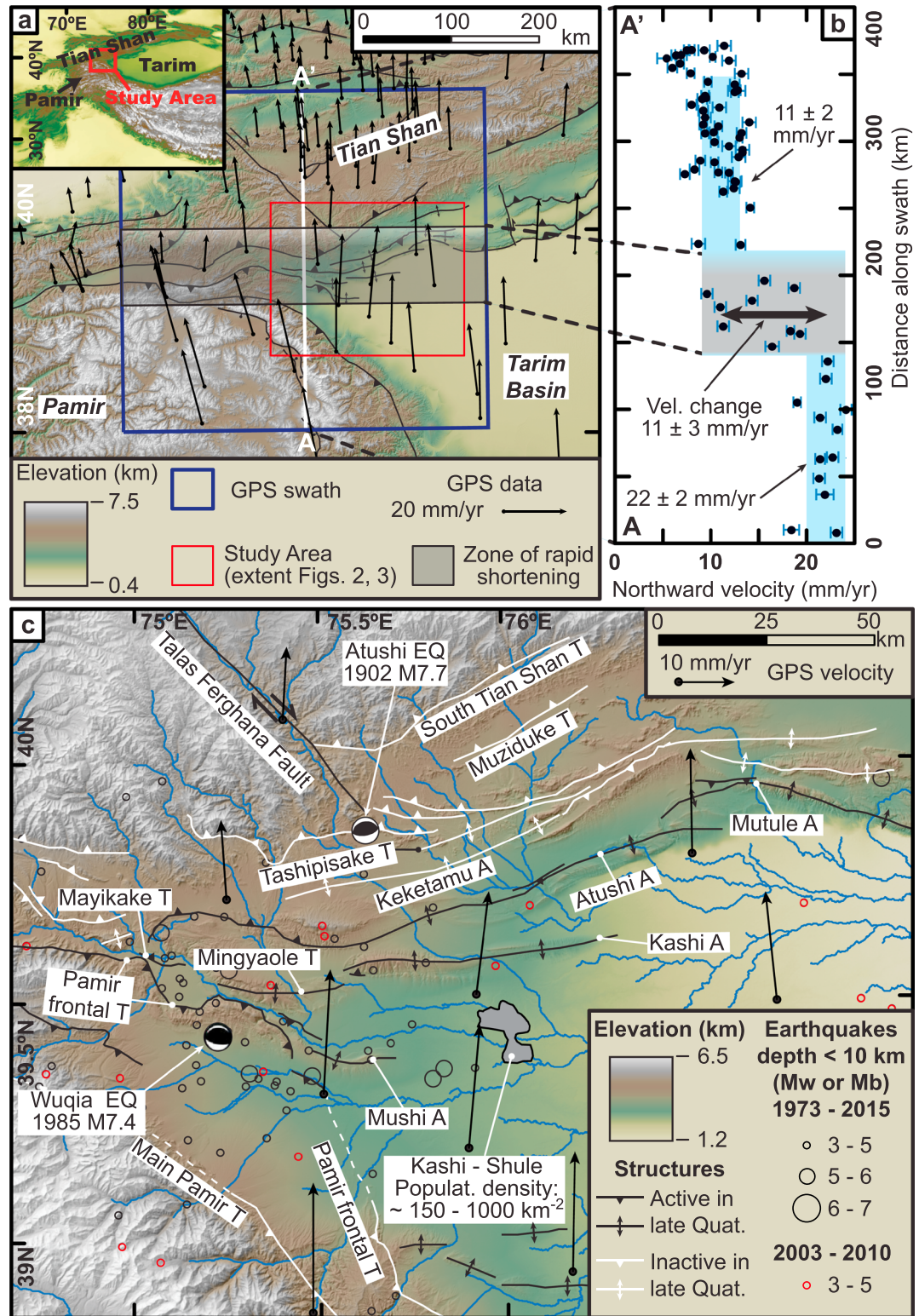


Figure 1. Overview of the study area. (a) Regional map of the Pamir and Tian Shan with horizontal GPS velocities [Zubovich et al., 2010]. (b) Northward component of the GPS velocity in the 400 km wide swath along A-A'. (c) Digital elevation model of the study area showing a series of faults and folds in the foreland of the Tian Shan and Pamir. Late Quaternary activity of structures (black and white lines) is based on geologic evidence published in previous studies [Chen et al., 2007; Heermance et al., 2008; Li et al., 2012, 2013, 2015; Thompson et al., 2015]. Earthquake locations are from the U.S. Geological Survey earthquake catalog except for the Wujia event [Feng, 1994] and the Kashi event [Kulikova, 2015]. A: anticline; T: thrust.

We compiled published initiation ages (0.4–1.6 Myr) and measured total structural relief (0.6–5.0 km) on published structural cross sections for the Mingyaole [Chen *et al.*, 2005; Li *et al.*, 2015], Kashi [Chen *et al.*, 2007], Atushi [Scharer *et al.*, 2004; Heermance *et al.*, 2008], Mushi [Li *et al.*, 2013; Thompson, 2013], and Mutule [Bufe *et al.*, 2017] folds (Table S3 and Figure S8). As an exception, initiation of the Mutule fold was estimated from the published initiation age of the Atushi fold to the west [Chen *et al.*, 2002; Scharer *et al.*, 2004; Heermance *et al.*, 2008] on the basis of interference between the two structures (Table S3). To account for uncertainties in the position of the outermost hinges and strata thickness, we assign a 2σ uncertainty of ± 500 m to all measurements of total structural relief estimated from geologic cross sections (Table S3 and Figure S8). For each structure, total rock uplift was then divided by the initiation age to obtain an average uplift rate since initiation of growth (Table S3). Finally, we compiled published ages (8.5–80 kyr) and heights above the modern river (15–130 m) for uplifted Late Quaternary fluvial deposits that are largely unaffected by erosion and can be assumed equivalent to record both rock and surface uplift [Heermance *et al.*, 2008; Li *et al.*, 2012, 2013; Thompson, 2013; Li *et al.*, 2015; Bufe *et al.*, 2017] (Table S3). For terraces with ages obtained through both fine-grained quartz optically stimulated luminescence [Li *et al.*, 2012] and cosmogenic radionuclide (CRN) dating [Thompson, 2013], we used the CRN dates, because they have been shown to be more reliable in this region [Thompson, 2013].

A comparison of uplift rates among multiple structures assumes a common base level. Geologic uplift rates of thrust faults and folds are calculated, where possible, with respect to the surrounding basins (e.g., Figure S8). Modern rivers serve as references for river terrace heights used to estimate uplift rates of folds at kiloyear timescales. These references are assumed to be equivalent to the reference of the modern river. In turn, InSAR vertical velocities have to be recalculated with respect to the basins in the study area. To this end, we estimate the vertical motions of these basins with respect to stable Eurasia using swath profiles drawn perpendicular to the strike of major structures (Figures S6 and S7). An estimated background uplift rate of 1.5 ± 0.5 mm/yr is fairly consistent across the study area and is subtracted from the InSAR rates when they are compared to geologic uplift rates (Table S2).

4. Results

The decomposition of the InSAR time series clearly resolves 10 to 20 km wide zones of surface uplift centered along nearly all structures in the study area that are interpreted or known to have been active during the Quaternary (Figure 2). These vertical velocities on active structures are smooth across track boundaries (Figure 2) and consistent with a recent independently published decomposition of InSAR in the region [Qiao *et al.*, 2017]. Systematic correlation between InSAR velocities and topography can arise from atmospheric phase delays. The lack of correlation of vertical InSAR velocities with many major topographic features (Figures 3, S6, and S7), however, supports the interpretation of a tectonic origin for those structures that do show elevated surface uplift rates. The large, elliptical uplift signal along the western part of the Keketamu anticline north of Atushi (Figure 2) is present in only one track (Figures S3 and S4) and could arise from atmospheric phase delays. Alternatively, the signal could be linked to water injection into the Akmomu gas field (Figure 2). Significant subsidence centered on the cities of Kashi and Shule (Figure 2) is probably due to groundwater withdrawal.

We find that surface uplift rates are highest along the Pamir Frontal Thrust (PFT), the Mushi anticline, and the Kashi anticline (Figure 2). Our data might indicate ongoing uplift along the South Tian Shan Thrust, but the Main Pamir Thrust, as well as the Tian Shan foreland north and east of the Atushi fold (including the Mutule fold), appear to be inactive (Figure 2). Modest earthquakes ($M \leq 5$) that occurred between 2003 and 2010 and depths of 9–10 km (Figure 2) are neither known nor expected to have produced surface displacements larger than the sensitivity of the InSAR (>4 –10 cm over 7 years) [Bonilla, 1982; Biasi and Weldon, 2006]. Whereas slip rate variations during a seismic cycle could introduce uncertainties [Thatcher, 1984; Cattin and Avouac, 2000; Hilley *et al.*, 2009], the observed uplift pattern is consistent with constraints on longer-term geologic uplift rates (Figure 3), as well as inferred basinward propagation of the deformation front over the past 25 Myr [Heermance *et al.*, 2008; Chen *et al.*, 2011; Thompson *et al.*, 2015].

Six-kilometer wide swaths aligned along the axis of each active structure reveal significant spatial variations in decadal surface uplift rates (Figure 3). The Kashi and Atushi folds show a broad, bow-shaped pattern with peak rates close to their centers (Figure 3). Surface uplift rates decrease at the tips of the folds with a tip-zone

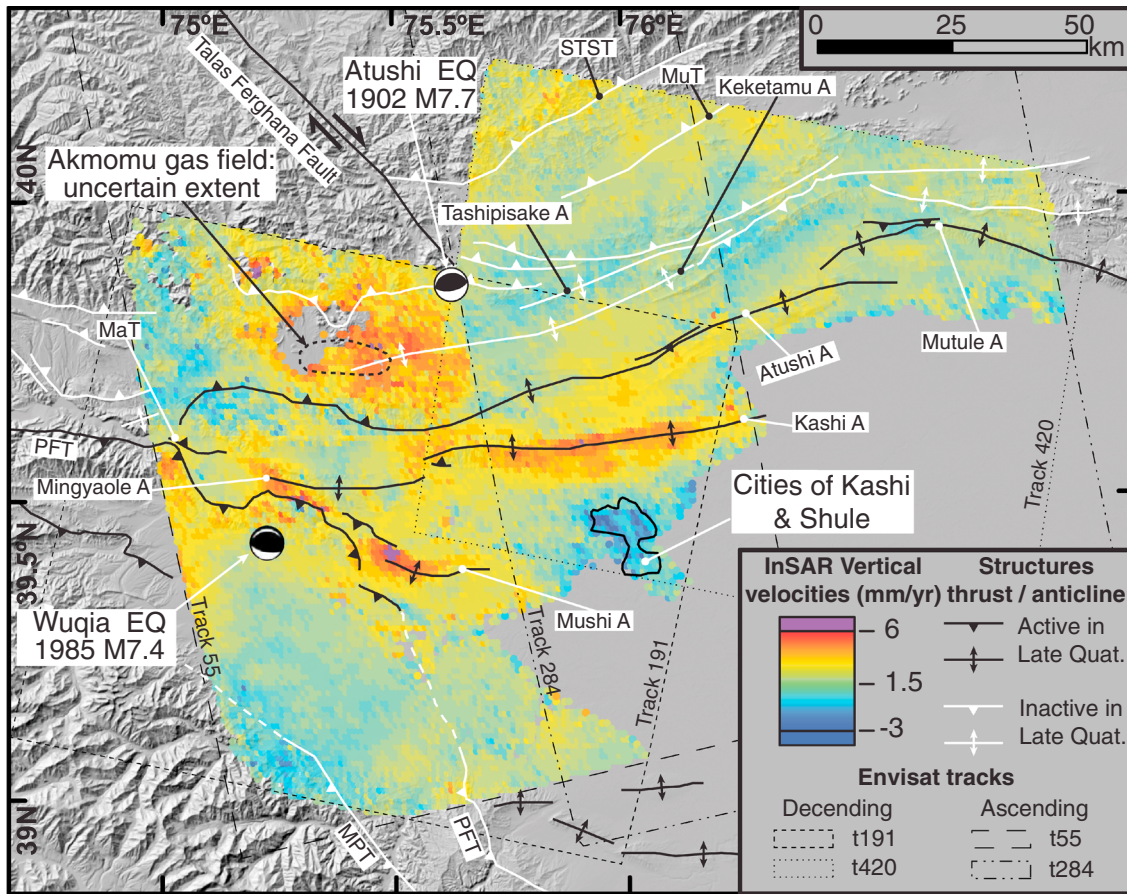


Figure 2. Decadal uplift rates from InSAR time series analysis of Envisat data for two ascending and two descending tracks. PFT: Pamir Frontal Thrust; MPT: Main Pamir Thrust; MaT: Mayikake Thrust; MuT: Muziduke Thrust; STST: South Tian Shan Thrust. A: anticline.

spanning 10–25% of the length of the structure. Similar to these two structures, the Mushi fold also shows peak surface uplift rates close to its center, but the peak is narrower and higher. Whereas postseismic effects from the nearby 1985 M7.4 Wuqia earthquake to the west of Mushi (Figure 2) cannot be ruled out, the gradual decrease of surface uplift rates toward the eastern tip of the fold is consistent with observed lateral tilting of fluvial terraces since at least 130 ka [Li et al., 2013]. In contrast to these well-defined patterns, spatial surface variations of uplift rate along the PFT and the Mingyaole fold are more complex. Uncertainties in the InSAR data, interference of structures, and fault segmentation could cause these variations. Thus, possibly, the tips of the Mingyaole fold uplift faster due to interference with the Kashi fold (to the east) and the PFT (to the west).

Assuming that peak decadal surface uplift rates on major structures are dominated by rock uplift, as described above, we find that average rock uplift rates measured (1) since fold-initiation, (2) across the last 10–80 kyr, and (3) across a 7 year (InSAR) interval have either stayed constant or have increased along frontal structures: the PFT and the Mushi and Kashi folds (Figures 4 and S9). In contrast, rock uplift rates on the more hinterland Mutule and Atushi folds have decreased (Figures 4 and S9). Such spatial patterns are consistent with basinward propagation of peak strain rates [Heermance et al., 2008; Thompson et al., 2015].

5. Monte Carlo Modeling of Gradually Changing Rock Uplift Rates

Changes in average rock uplift rate measured across different time intervals, which are each long enough to average across several earthquakes, are commonly obtained by linearly connecting single measurements of cumulative rock uplift [e.g., Gold and Cowgill, 2011] (Figure S10a). Such fits result in step-like changes in instantaneous uplift rates (Figure S10b). Sometimes, abrupt velocity changes can be linked to climatic or

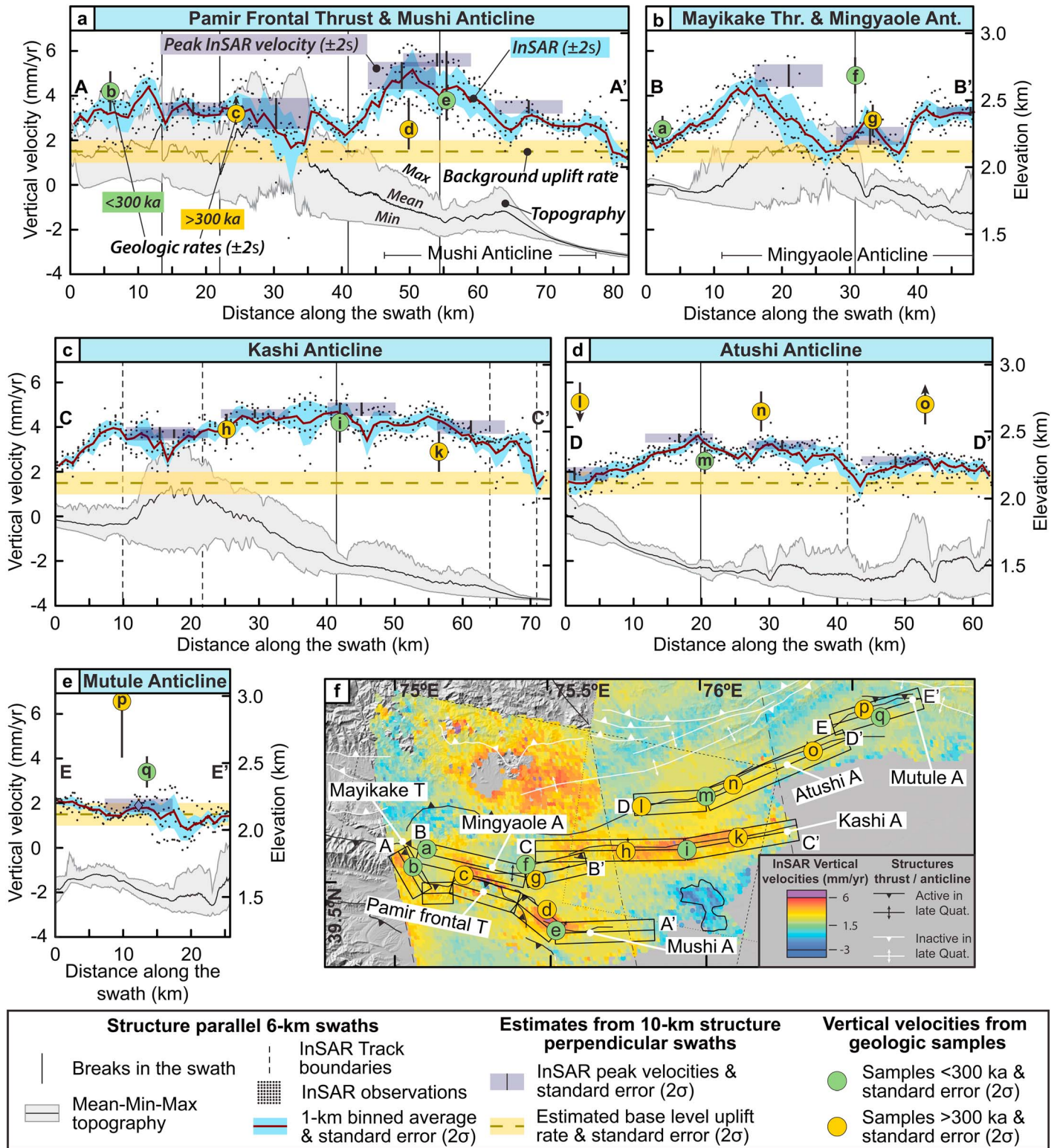


Figure 3. Along-strike changes in rock uplift rates. (a–e) Six kilometer wide swath profiles along strike of the study area’s major active structures show decadal vertical velocities and associated topography. Mean and standard error of the InSAR velocities are calculated in 1 km bins (approximate spacing of points in the InSAR velocity map). Yellow horizontal bars mark background uplift rate of 1.5 ± 0.5 ($\pm 2\sigma$) mm/yr (see text and Figures S6 and S7). Peak geodetic uplift rates ($\pm 2\sigma$) were measured on these same swaths (Figures S6 and S7). Yellow and green points are geologic uplift rates compiled from the published literature (Table S3). For illustration purposes, the background uplift rate in the InSAR velocity field was added to the geologic rates (Table S3). (f) Overview map with profile locations and locations where geologic uplift rates were calculated. A: anticline; T: thrust.

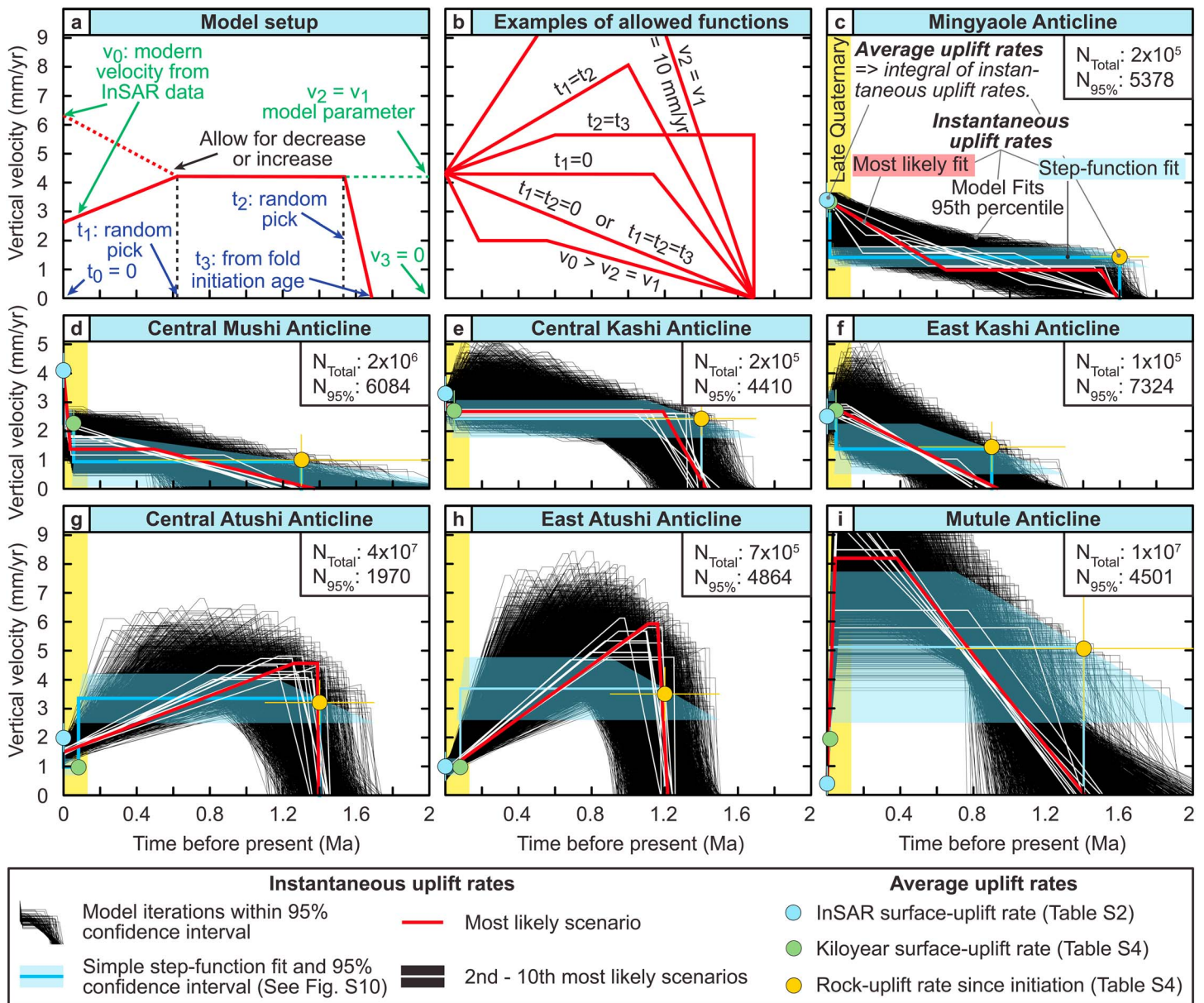


Figure 4. Results from uplift rate modeling on Mingyaole, Mushi, Kashi, Atushi, and Mutule. (a) Conceptual sketch showing all model parameters. (b) Examples of functional forms allowed by the model. (c–i) Results from modeling showing all scenarios with probabilities within 5% of the maximum probability (black lines). The single most likely scenario is shown in red. The next nine most likely scenarios are shown in white. A step-function fit is shown in blue. Green and yellow data points are average geologic rock uplift rates from the published literature (Table S3), and blue data points are average geodetic rock uplift rates from this InSAR study (Table S2). All average rates are plotted at the time equivalent to the length of the averaging period. N_{total} is the total number of iterations per run, and $N_{95\%}$ is the number of iterations within the 95% confidence interval. The yellow bar ranging to 130 kyr denotes the range of the Late Quaternary. All model fits can also be plotted as cumulative displacement versus time (Figure S11).

geologic triggers [Hampel et al., 2007; Gold et al., 2017]. Even if such changes occurred, however, their precise timing is difficult to capture where few sample ages exist. Moreover, gradual changes in deformation velocity of single structures can occur [Gourmelen et al., 2011], for example, from the lateral propagation of a structure with instantaneous rock uplift rates that drop smoothly to 0 toward the tip (Figures 3a, 3c, 3d, S10c, and S10d). Even structures lacking propagating tips might accelerate after initiation and decelerate toward the cessation of deformation [Gourmelen et al., 2011] or vary in a complex sequence of accelerations and decelerations [Chevalier et al., 2005; Gunderson et al., 2014]. Such gradual changes can only be detected in high-resolution uplift rate data sets obtained, for example, from well-dated terraces [Bourgeois et al., 2007].

An unlimited number of functions can be fit to discrete rock uplift data calculated across different time intervals (Figure S10a). Therefore, in addition to fitting step functions to our data, we explore the range of plausible gradual uplift rate evolutions for five selected structures by imposing a geologically reasonable piecewise linear function with an initial phase of velocities increasing from 0 ($v_3 = 0$) at the time of initiation (t_3) to an intermediate value (v_2) at some unknown time (t_2) (Figure 4a), followed by a time of steady velocities ($v_1 = v_2$) and either an increase or decrease at time (t_1) to the final velocity (v_0) at the modern day ($t_0 = 0$) (Figure 4a). Using a Monte Carlo approach, we randomly pick a parameter set for each of at least 10^5 iterations (Figure 4 and Table S4) and evaluate the goodness of fit of the resulting uplift rate scenario to the geologic data (see text S2 for additional details). We note that t_1 and t_2 are each allowed to be 0, equal to t_3 , or equal to each other, which includes a range of scenarios such as step functions (Figure 4b). However, only one time period is allowed across which velocities are constant, and functions with more complex step changes cannot be fit with our approach. This limit may bias the model toward fitting gradual rate changes in situations for which the three mean uplift rates define inconsistent rate changes through time, e.g., a velocity increase followed by a decrease (Figure 4f) or vice versa (Figure 4g).

For all folds, curves within 95% of the maximum probability show a variety of likely uplift rate scenarios (Figures 4 and S11). For structures for which average rock uplift rates calculated across different time intervals are similar in magnitude (within $< \sim 1$ mm/yr), near-step-like functions of instantaneous uplift rates yield the best fits, but initial acceleration periods of a few tens to hundreds of kiloyears are not unlikely (Central Kashi: Figures 4e and S12a). In contrast, where average uplift rates measured across Late Quaternary timescales have increased compared to the rate since initiation of the structure, a more gradual change in uplift rate through time is predicted by a higher fraction of model solutions (Mushi, Mingyaole, Eastern Kashi: Figures 4c, 4d, 4f, and S12b). Finally, where uplift rates have decreased significantly over time, a rapid increase in velocities, followed by a gradual decrease, is among the best solutions of the model (Atushi-Mutule: Figures 4g–4i and S12c).

6. Discussion

In this study, decomposition of InSAR data resolves surface uplift rates of individual ≤ 10 km wide structures over the past decade along the Tian Shan-Pamir interface in unprecedented detail. The correlation of decadal surface uplift rates with geologic outlines of the structures, the absence of a strong correlation between elevation and InSAR velocities, the consistency of peak surface uplift rates across track boundaries, and their smooth variation along structures support the interpretation of a tectonic origin for the InSAR signal on the PFT and the Mushi, Mingyaole, Kashi, Atushi, and Mutule folds (Figure 2). The consistency between the broad spatial patterns of geologic and geodetic uplift rates on the structures (Figure 3) suggests that large-scale (greater than tens of kilometers) patterns of decadal velocities can inform longer-term trends. However, it remains problematic to assess the effects of short-term velocity variations due, for example, to changes across an earthquake cycle, with such a simple rate comparison. Our data confirm previous findings of the basinward propagation of tectonic activity and lend further support to the assumed, but debated, inactivity of the Main Pamir Thrust [Sobel *et al.*, 2011; Li *et al.*, 2012; Thompson *et al.*, 2015] and of the northern Tian Shan foreland [Heermance *et al.*, 2008].

The background surface uplift rate of 1.5 ± 0.5 mm/yr (Figures 2, S6, and S7) arises from tying the InSAR data to the stable Eurasian reference frame using GPS data (Text S1). Because the rate is within uncertainties of the GPS vertical velocities (> 2 mm/yr), its significance remains unknown. Here for all analyses, the background rate is subtracted from the InSAR measurements and does not affect the comparison between InSAR and geologic rates.

The arc-shaped spatial pattern of decadal surface and rock uplift rates along the Kashi, Atushi, and Mushi folds with “tip zones” in which vertical velocities are smoothly dropping to 0 (Figure 3) is inconsistent with a pure block shape model of incremental surface uplift [Manighetti *et al.*, 2001]. Instead, it favors interpretations in which uplift rates change more gradually along strike (Figure S10). Where such gradual, along-strike changes occur, lateral propagation of tip zones can lead to temporal changes of instantaneous uplift rates for any point through which the tip propagates (Figure S10c and S10d). Lateral propagation rates of ~ 40 and ~ 50 mm/yr have been inferred for the tips of the Kashi and Atushi folds, respectively [Scharer *et al.*, 2004; Chen *et al.*, 2007]. Thus, with a tip zone length of 10 ± 5 km, and assuming that this spatial pattern was

constant through time, a point on the Kashi or Atushi fold would be expected to accelerate for at least 200 ± 100 kyr or 250 ± 130 kyr, respectively. Such timescales of acceleration are consistent with the modeled uplift rate scenarios (Figure 4), although some of the most probable fits to the Atushi data predict shorter periods of acceleration (Figures 4f and 4g).

Where structures interfere (Mingyaole fold), are segmented (PFT), or tilt laterally (Mushi fold), the spatial pattern of decadal uplift rates is more complicated (Figure 3) and such complexity makes the interpretation of a “representative” modern velocity challenging. Moreover, with only three data points for uplift rates across a time interval of 0.5–1.6 Myr on any given fold, considerable uncertainties remain on a fold’s temporal uplift rate evolution. Nevertheless, our modeling framework yields ranges of probable temporal variations in uplift rates that are distinct for different structures and can constrain a range of likely kinematic evolution of contractional structures.

7. Conclusions

With a decomposition of InSAR data, we obtain insights into the spatial patterns of decadal surface and rock uplift rates along rapidly deforming contractional structures at the Tian Shan–Pamir interface and observe spatial patterns of fold uplift that are inconsistent with block-like deformation patterns. We compile published geologic uplift rates and use stepwise and piecewise linear fitting of geodetic and geologic uplift rates to reveal temporal patterns of deformation in the study area. Our observations confirm the propagation of deformation away from the mountain fronts and into the Tarim Basin over the past 2 Myr.

Acknowledgments

We acknowledge ESA for providing the ASAR images and technical support. This work benefited from discussions with Tim Wright, Daniel Wissmann, Miriam Dünforth, Cengiz Yildirim, Steffanie Rieger, and Markus Hoffmann. Careful reviews of the work by Romain Jolivet, Ryan Gold, and an anonymous reviewer improved an early version. A DAAD graduate student award and a UCSB Regents Special Fellowship to A.B., as well as National Science Foundation grant 1050070 to D.W.B. and B.B. and the LED2016A05 grant to C.J., L.T., and L.L., are gratefully acknowledged. D.P.S.B. was sponsored by the Jet Propulsion Laboratory, California Institute of Technology, under a contract with the National Aeronautics and Space Administration. Shapefiles of interferometric data as well as codes for the Monte Carlo modeling can be found in the supporting information. Additional detail and primary sources for the geologic data used in the analysis are included in Figure S8 and Table S3.

References

- Abdrakhmatov, K. Y., et al. (1996), Relatively recent construction of the Tien Shan inferred from GPS measurements of present-day crustal deformation rates, *Nature*, *384*(6608), 450–453, doi:10.1038/384450a0.
- Allen, M., J. Jackson, and R. Walker (2004), Late Cenozoic reorganization of the Arabia–Eurasia collision and the comparison of short-term and long-term deformation rates, *Tectonics*, *23*, TC2008, doi:10.1029/2003TC001530.
- Allmendinger, R. W. (1998), Inverse and forward numerical modeling of trishear fault-propagation folds, *Tectonics*, *17*(4), 640–656, doi:10.1029/98TC01907.
- Amos, C. B., D. W. Burbank, and S. A. L. Read (2010), Along-strike growth of the Ostler fault, New Zealand: Consequences for drainage deflection above active thrusts, *Tectonics*, *29*, TC4021, doi:10.1029/2009TC002613.
- Anders, M. H., and R. W. Schlische (1994), Overlapping faults, intrabasin highs, and the growth of normal faults, *J. Geol.*, *102*(2), 165–179.
- Bekaert, D. P. S., A. Hooper, and T. J. Wright (2015a), A spatially variable power law tropospheric correction technique for InSAR data, *J. Geophys. Res. Solid Earth*, *120*, 1345–1356, doi:10.1002/2014JB011558.
- Bekaert, D. P. S., R. J. Walters, T. J. Wright, A. J. Hooper, and D. J. Parker (2015b), Statistical comparison of InSAR tropospheric correction techniques, *Remote Sens. Environ.*, *170*, 40–47, doi:10.1016/j.rse.2015.08.035.
- Bettinelli, P., J.-P. Avouac, M. Flouzat, L. Bollinger, G. Ramillien, S. Rajaure, and S. Sapkota (2008), Seasonal variations of seismicity and geodetic strain in the Himalaya induced by surface hydrology, *Earth Planet. Sci. Lett.*, *266*(3–4), 332–344, doi:10.1016/j.epsl.2007.11.021.
- Biasi, G. P., and R. J. Weldon (2006), Estimating surface rupture length and magnitude of paleoearthquakes from point measurements of rupture displacement, *Bull. Seismol. Soc. Am.*, *96*(5), 1612–1623, doi:10.1785/0120040172.
- Bonilla, M. G. (1982), Evaluation of potential surface faulting and other tectonic deformation, *U.S. Geol. Surv. Open File Rep.*, *82-0732*, 91 pp.
- Bourgeois, J., F. Bigot-Cormier, D. Bourles, R. Braucher, O. Dauteuil, C. Witt, and F. Michaud (2007), Tectonic record of strain buildup and abrupt coseismic stress release across the northwestern Peru coastal plain, shelf, and continental slope during the past 200 kyr, *J. Geophys. Res.*, *112*, B04104, doi:10.1029/2006JB004491.
- Bufe, A., D. W. Burbank, L. Liu, B. Bookhagen, J. Qin, J. Chen, J. A. Thompson Jobe, and H. Yang (2017), Variations of lateral bedrock erosion rates control planation of uplifting folds in the foreland of the Tian Shan, NW China, *J. Geophys. Res. Earth Surf.*, doi:10.1002/2016JF004099.
- Burbank, D., A. Meigs, and N. Brozović (1996), Interactions of growing folds and coeval depositional systems, *Basin Res.*, *8*(3), 199–223, doi:10.1046/j.1365-2117.1996.00181.x.
- Cattin, R., and J. P. Avouac (2000), Modeling mountain building and the seismic cycle in the Himalaya of Nepal, *J. Geophys. Res.*, *105*(B6), 13,389–13,407, doi:10.1029/2000JB900032.
- Chen, J., D. W. Burbank, K. M. Scharer, E. Sobel, J. Yin, C. Rubin, and R. Zhao (2002), Magnetochronology of the Upper Cenozoic strata in the Southwestern Chinese Tian Shan: Rates of Pleistocene folding and thrusting, *Earth Planet. Sci. Lett.*, *195*(1–2), 113–130, doi:10.1016/S0012-821X(01)00579-9.
- Chen, J., K. Scharer, D. Burbank, R. Heermance, and C.-S. Wang (2005), Quaternary detachment folding of the Mingyaole anticline, southwestern Tian Shan, *Dizhen Dizhi Seismol. Geol.*, *27*(4), 530–547.
- Chen, J., R. Heermance, D. W. Burbank, K. M. Scharer, J. Miao, and C. Wang (2007), Quantification of growth and lateral propagation of the Kashi anticline, southwest Chinese Tian Shan, *J. Geophys. Res.*, *112*, B03S16, doi:10.1029/2006JB004345.
- Chen, J., T. Li, W.-q. Li, and Z.-d. Yuan (2011), Late Cenozoic and present tectonic deformation in the Pamir salient, northwestern China, *Seismol. Geol.*, *33*(2).
- Chevalier, M.-L., F. J. Ryerson, P. Tapponnier, R. C. Finkel, J. Van Der Woerd, L. Haibing, and L. Qing (2005), Slip-rate measurements on the Karakorum Fault may imply secular variations in fault motion, *Science*, *307*(5708), 411–414, doi:10.1126/science.1105466.
- Clark, M. K. (2012), Continental collision slowing due to viscous mantle lithosphere rather than topography, *Nature*, *483*(7387), 74–77, doi:10.1038/nature10848.
- Davis, K., D. W. Burbank, D. Fisher, S. Wallace, and D. Nobes (2005), Thrust-fault growth and segment linkage in the active Ostler fault zone, New Zealand, *J. Struct. Geol.*, *27*(8), 1528–1546, doi:10.1016/j.jsg.2005.04.011.

- Dawers, N. H., M. H. Anders, and C. H. Scholz (1993), Growth of normal faults: Displacement-length scaling, *Geology*, 21(12), 1107–1110, doi:10.1130/0091-7613(1993)021<1107:gonfdl>2.3.co;2.
- Dee, D. P., et al. (2011), The ERA-Interim reanalysis: Configuration and performance of the data assimilation system, *Q. J. R. Meteorol. Soc.*, 137(656), 553–597, doi:10.1002/qj.828.
- Dolan, J. F., D. D. Bowman, and C. G. Sammis (2007), Long-range and long-term fault interactions in Southern California, *Geology*, 35(9), 855–858, doi:10.1130/g23789a.1.
- Epard, J. L., and R. H. Groshong Jr. (1995), Kinematic model of detachment folding including limb rotation, fixed hinges and layer-parallel strain, *Tectonophysics*, 247(1–4), 85–103, doi:10.1016/0040-1951(94)00266-C.
- Farr, T. G., et al. (2007), The Shuttle Radar Topography Mission, *Rev. Geophys.*, 45, RG2004, doi:10.1029/2005RG000183.
- Feng, X. (1994), Surface rupture associated with the 1985 Wuqia earthquake, in *Xinjiang: Research on Active Fault*, pp. 45–55, Seismological Press, Beijing.
- Friedrich, A. M., B. P. Wernicke, N. A. Niemi, R. A. Bennett, and J. L. Davis (2003), Comparison of geodetic and geologic data from the Wasatch region, Utah, and implications for the spectral character of Earth deformation at periods of 10 to 10 million years, *J. Geophys. Res.*, 108(B4), 2199, doi:10.1029/2001JB000682.
- Gold, R. D., and E. Cowgill (2011), Deriving fault-slip histories to test for secular variation in slip, with examples from the Kunlun and Awatere faults, *Earth Planet. Sci. Lett.*, 301(1–2), 52–64, doi:10.1016/j.epsl.2010.10.011.
- Gold, R. D., A. Friedrich, S. Kübler, and M. Salamon (2017), Apparent late Quaternary fault-slip rate increase in the southern Lower Rhine graben, Central Europe, *Bull. Seismol. Soc. Am.*, doi:10.1785/0120160197.
- Gourmelen, N., T. H. Dixon, F. Amelung, and G. Schmalzle (2011), Acceleration and evolution of faults: An example from the Hunter Mountain–Panamint Valley fault zone, eastern California, *Earth Planet. Sci. Lett.*, 301(1–2), 337–344, doi:10.1016/j.epsl.2010.11.016.
- Grant, L. B., and K. Sieh (1994), Paleoseismic evidence of clustered earthquakes on the San Andreas Fault in the Carrizo Plain, California, *J. Geophys. Res.*, 99(B4), 6819–6841, doi:10.1029/94JB00125.
- Gunderson, K. L., et al. (2014), Unraveling tectonic and climatic controls on synorogenic growth strata (Northern Apennines, Italy), *Geol. Soc. Am. Bull.*, 126(3–4), 532–552, doi:10.1130/b30902.1.
- Hampel, A., R. Hetzel, and A. L. Densmore (2007), Postglacial slip-rate increase on the Teton normal fault, northern Basin and Range Province, caused by melting of the Yellowstone ice cap and deglaciation of the Teton Range?, *Geology*, 35(12), 1107–1110, doi:10.1130/g24093a.1.
- Heermance, R. V., J. Chen, D. W. Burbank, and J. Miao (2008), Temporal constraints and pulsed Late Cenozoic deformation during the structural disruption of the active Kashi foreland, northwest China, *Tectonics*, 27, TC6012, doi:10.1029/2007TC002226.
- Hilley, G. E., and J. R. Arrowsmith (2008), Geomorphic response to uplift along the Dragon's Back pressure ridge, Carrizo Plain, California, *Geology*, 36(5), 367–370, doi:10.1130/g24517a.1.
- Hilley, G. E., K. M. Johnson, M. Wang, Z.-K. Shen, and R. Bürgmann (2009), Earthquake-cycle deformation and fault slip rates in northern Tibet, *Geology*, 37(1), 31–34, doi:10.1130/g25157a.1.
- Hooper, A., D. Bekaert, K. Spaans, and M. Arkan (2012), Recent advances in SAR interferometry time series analysis for measuring crustal deformation, *Tectonophysics*, 514–517, 1–13, doi:10.1016/j.tecto.2011.10.013.
- Hooper, A., H. Zebker, P. Segall, and B. Kampes (2004), A new method for measuring deformation on volcanoes and other natural terrains using InSAR persistent scatterers, *Geophys. Res. Lett.*, 31, L23611, doi:10.1029/2004GL021737.
- Hubert-Ferrari, A., J. Suppe, R. Gonzalez-Mieres, and X. Wang (2007), Mechanisms of active folding of the landscape (southern Tian Shan, China), *J. Geophys. Res.*, 112, B03S09, doi:10.1029/2006JB004362.
- Hussain, E., A. Hooper, T. J. Wright, R. J. Walters, and D. P. S. Bekaert (2016a), Interseismic strain accumulation across the central North Anatolian Fault from iteratively unwrapped InSAR measurements, *J. Geophys. Res. Solid Earth*, 121, 9000–9019, doi:10.1002/2016JB013108.
- Hussain, E., T. J. Wright, R. J. Walters, D. Bekaert, A. Hooper, and G. A. Houseman (2016b), Geodetic observations of postseismic creep in the decade after the 1999 Izmit earthquake, Turkey: Implications for a shallow slip deficit, *J. Geophys. Res. Solid Earth*, 121, 2980–3001, doi:10.1002/2015JB012737.
- Jackson, J., J.-F. Ritz, L. Siame, G. Raisbeck, F. Yiou, R. Norris, J. Youngson, and E. Bennett (2002), Fault growth and landscape development rates in Otago, New Zealand, using in situ cosmogenic ¹⁰Be, *Earth Planet. Sci. Lett.*, 195(3–4), 185–193, doi:10.1016/S0012-821X(01)00583-0.
- Kampes, B., and S. Usai (1999), Doris: The delft object-oriented radar interferometric software, in *2nd International Symposium on Operationalization of Remote Sensing*, Enschede, Netherlands.
- Kulikova, G. (2015), Source parameters of the major historical earthquakes in the Tien-Shan region from the late 19th to the early 20th century, Univ. of Potsdam, Germany.
- Li, T., J. Chen, J. A. Thompson, D. W. Burbank, and W. Xiao (2012), Equivalency of geologic and geodetic rates in contractional orogens: New insights from the Pamir Frontal Thrust, *Geophys. Res. Lett.*, 39, L15305, doi:10.1029/2012GL051782.
- Li, T., J. Chen, J. A. Thompson, D. W. Burbank, and X. Yang (2013), Quantification of three-dimensional folding using fluvial terraces: A case study from the Mushi anticline, northern margin of the Chinese Pamir, *J. Geophys. Res. Solid Earth*, 118, 4628–4647, doi:10.1002/jgrb.50316.
- Li, T., J. Chen, J. A. Thompson, D. W. Burbank, and H. Yang (2015), Hinge-migrated fold-scarp model based on an analysis of bed geometry: A study from the Mingyao anticline, southern foreland of Chinese Tian Shan, *J. Geophys. Res. Solid Earth*, 120, 6592–6613, doi:10.1002/2015JB012102.
- Manighetti, I., G. C. P. King, Y. Gaudemer, C. H. Scholz, and C. Doubre (2001), Slip accumulation and lateral propagation of active normal faults in Afar, *J. Geophys. Res.*, 106(B7), 13,667–13,696, doi:10.1029/2000JB900471.
- Marco, S., M. Stein, A. Agnon, and H. Ron (1996), Long-term earthquake clustering: A 50,000-year paleoseismic record in the Dead Sea Graben, *J. Geophys. Res.*, 101(B3), 6179–6191, doi:10.1029/95JB01587.
- Meade, B. J., and B. H. Hager (2004), Viscoelastic deformation for a clustered earthquake cycle, *Geophys. Res. Lett.*, 31, L10610, doi:10.1029/2004GL019643.
- Molnar, P., and J. M. Stock (2009), Slowing of India's convergence with Eurasia since 20 Ma and its implications for Tibetan mantle dynamics, *Tectonics*, 28, TC3001, doi:10.1029/2008TC002271.
- Oskin, M., L. Perg, D. Blumentritt, S. Mukhopadhyay, and A. Iriondo (2007), Slip rate of the Calico fault: Implications for geologic versus geodetic rate discrepancy in the Eastern California Shear Zone, *J. Geophys. Res.*, 112, B03402, doi:10.1029/2006JB004451.
- Oskin, M., L. Perg, E. Shelef, M. Strane, E. Gurney, B. Singer, and X. Zhang (2008), Elevated shear zone loading rate during an earthquake cluster in eastern California, *Geology*, 36(6), 507–510, doi:10.1130/g24814a.1.
- Poblet, J., and K. McClay (1996), Geometry and kinematics of single-layer detachment folds, *AAPG Bull.*, 80(7), 1085–1109.
- Qiao, X., P. Yu, Z. Nie, J. Li, X. Wang, S. I. Kuzikov, Q. Wang, and S. Yang (2017), The crustal deformation revealed by GPS and InSAR in the northwest corner of the Tarim Basin, northwestern China, *Pure Appl. Geophys.*, 1–19, doi:10.1007/s00024-017-1473-6.

- Rosen, P. A., S. Hensley, G. Peltzer, and M. Simons (2004), Updated repeat orbit interferometry package released, *Eos Trans. AGU*, 85(5), 47–47, doi:10.1029/2004EO050004.
- Scharer, K. M., D. W. Burbank, J. Chen, R. J. Weldon, C. Rubin, R. Zhao, and J. Shen (2004), Detachment folding in the Southwestern Tian Shan–Tarim foreland, China: Shortening estimates and rates, *J. Struct. Geol.*, 26(11), 2119–2137, doi:10.1016/j.jsg.2004.02.016.
- Sobel, E. R., J. Chen, and R. V. Heermance (2006), Late Oligocene–Early Miocene initiation of shortening in the Southwestern Chinese Tian Shan: Implications for Neogene shortening rate variations, *Earth Planet. Sci. Lett.*, 247(1–2), 70–81, doi:10.1016/j.epsl.2006.03.048.
- Sobel, E. R., L. M. Schoenbohm, J. Chen, R. Thiede, D. F. Stockli, M. Sudo, and M. R. Strecker (2011), Late Miocene–Pliocene deceleration of dextral slip between Pamir and Tarim: Implications for Pamir orogenesis, *Earth Planet. Sci. Lett.*, 304(3–4), 369–378, doi:10.1016/j.epsl.2011.02.012.
- Suppe, J. (1983), Geometry and kinematics of fault-bend folding, *Am. J. Sci.*, 283(7), 684–721.
- Suppe, J., and D. A. Medwedeff (1990), Geometry and kinematics of fault-propagation folding, *Eclogae Geol. Helv.*, 83(3), 409–454.
- Thatcher, W. (1984), The earthquake deformation cycle, recurrence, and the time-predictable model, *J. Geophys. Res.*, 89(B7), 5674–5680, doi:10.1029/JB089iB07p05674.
- Thompson, J. A. (2013), Neogene tectonic evolution of the NE Pamir margin, NW China, Univ. of California, Santa Barbara, Calif.
- Thompson, J. A., D. W. Burbank, T. Li, J. Chen, and B. Bookhagen (2015), Late Miocene northward propagation of the northeast Pamir thrust system, northwest China, *Tectonics*, 34, 510–534, doi:10.1002/2014TC003690.
- Thompson, S. C., R. J. Weldon, C. M. Rubin, K. Abdrakhmatov, P. Molnar, and G. W. Berger (2002), Late Quaternary slip rates across the central Tien Shan, Kyrgyzstan, central Asia, *J. Geophys. Res.*, 107(B9), 2203, doi:10.1029/2001JB000596.
- Yan, D.-P., Y.-B. Xu, Z.-B. Dong, L. Qiu, S. Zhang, and M. Wells (2016), Fault-related fold styles and progressions in fold-thrust belts: Insights from sandbox modeling, *J. Geophys. Res. Solid Earth*, 121, 2087–2111, doi:10.1002/2015JB012397.
- Zubovich, A. V., et al. (2010), GPS velocity field for the Tien Shan and surrounding regions, *Tectonics*, 29, TC6014, doi:10.1029/2010TC002772.